nature portfolio

https://doi.org/10.1038/s41563-022-01238-w

Supplementary information

Bimorphic Floquet topological insulators

In the format provided by the authors and unedited

Supplementary Information

for

Bimorphic Floquet Topological Insulators

Georgios G. Pyrialakos[1,3*], Julius Beck[2*], Matthias Heinrich[2], Lukas J. Maczewsky[2], Nikolaos V. Kantartzis[3], Mercedeh Khajavikhan[4], Alexander Szameit[2] and Demetrios N. Christodoulides[1]

This document includes:

Supplementary Text

Supplementary Figures S1-S6

[1] College of Optics & Photonics-CREOL, University of Central Florida, Orlando, Florida 32816, USA. [2] Institute for Physics, University of Rostock, Albert-Einstein-Str. 23, 18059 Rostock, Germany. [3] Department of Electrical and Computer Engineering, Aristotle University of Thessaloniki, GR-54124 Thessaloniki, Greece. [4] Ming Hsieh Department of Electrical and Computer Engineering, University of Southern California, Los Angeles, CA, USA. [*] These authors contributed equally to this work. [‡] email: demetri@creol.ucf.edu

Supplementary Section S.I: *Chained lattice Hamiltonian and* 2×2 *effective model for the Dirac cone*

The unit cell of the honeycomb lattice comprises two principal elements (A and B) that form two independent sublattices connected by 180° rotational symmetry (Fig. S1). To preserve this symmetry the auxiliary elements are inserted symmetrically, at the center of each coupling path between elements A and B. The general form of the chained lattice Hamiltonian, accounting for all 5 sites, can be written as

$$H = \sum_{i,j} \beta_A \psi^{\dagger}_{\mathrm{A},i,j}\psi_{\mathrm{A},i,j} + \beta_B \psi^{\dagger}_{\mathrm{B},i,j}\psi_{\mathrm{B},i,j} + \beta_1 \psi^{\dagger}_{1,i,j}\psi_{1,i,j} + \beta_2 \psi^{\dagger}_{2,i,j}\psi_{2,i,j} + \beta_3 \psi^{\dagger}_{3,i,j}\psi_{3,i,j} \quad \text{(S1)}$$

$$+ \sum_{i,j} \left(c_{\mathrm{A1}} \psi^{\dagger}_{1,i,j}\psi_{\mathrm{A},i,j} + c_{\mathrm{B1}} \psi^{\dagger}_{1,i,j}\psi_{\mathrm{B},i,j-1} + c_{\mathrm{A2}} \psi^{\dagger}_{2,i,j}\psi_{\mathrm{A},i,j} + c_{\mathrm{B2}} \psi^{\dagger}_{2,i,j}\psi_{B,i,j} + c_{\mathrm{A3}} \psi^{\dagger}_{3,i,j}\psi_{\mathrm{A},i,j} + c_{\mathrm{B3}} \psi^{\dagger}_{3,i,j}\psi_{\mathrm{B},i-1,j} \right)$$

$$+ h.c$$

where $\psi^{\dagger}_{\mathrm{x},i,j}$ and $\psi_{\mathrm{x},i,j}$ are the creation and annihilation operations at site x and unit cell (i,j).

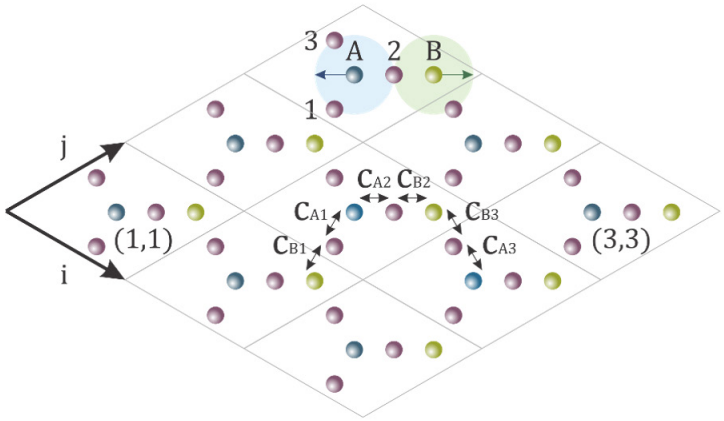

Figure S1: The chained lattice. Each unit cell of the extended lattice comprises 5 elements. The main elements A and B define two independent sublattices (shaded circles) connected by 180° rotational symmetry.

In the Hamiltonian of equation (S1), the on-site potentials (β) and the coupling terms (c) are time dependent variables. If the periodic variation involves a non-zero phase difference between the chains the unit cell becomes anisotropic, allowing the properties of the Dirac cones to freely vary in k space (i.e. the location, velocity and anisotropy of the cones are now independent variables). Meanwhile, it is not directly evident if the 5x5 system can host Dirac cones that can maintain a vanishing gap for the unit cell of Fig. S1, with fully anisotropic couplings and arbitrary on-site potentials on the chain elements.

The linear dispersion of a Dirac cone can be effectively captured by a 2×2 reduced Hamitonian, written in the following from

$$H(\mathbf{k}) = u^T \cdot (\boldsymbol{k} - \boldsymbol{k}_D) I + [u^D \cdot (\boldsymbol{k} - \boldsymbol{k}_D)]\boldsymbol{\sigma} + m'\sigma_z \quad \text{(S2)}$$

where $\boldsymbol{\sigma}$ are the Pauli matrices This equation involves the location ($\boldsymbol{k}_D$), dispersion velocity (u^D) and anisotropy (u^T) of the cone and also indicates the presence of a gap (for $m' \neq 0$). To extract a 2×2 effective representation of the system, we examine the three coupling paths between the main sites of the extended lattice as independent chains of three coupled elements. The set of equations describing this system is

$$\begin{aligned} \beta\psi_{\mathrm{A}} &= c_{\mathrm{A}i}\psi_i, \\ \beta\psi_i &= \beta_i\psi_i + c_{\mathrm{A}i}^*\psi_{\mathrm{A}} + c_{\mathrm{B}i}\psi_{\mathrm{B}}, \\ \beta\psi_{\mathrm{B}} &= c_{\mathrm{B}i}^*\psi_i, \end{aligned} \tag{S3}$$

where ψ_i is the field intensity at the auxiliary element in chain $i = 1,2,3$, β is the propagation constant as the system's eigenvalue, β_i a detuning constant of the middle element and $c_{A,Bi} = |c_{A,Bi}|e^{i\boldsymbol{k}\boldsymbol{r}_{A,Bi}}$. Here, $c_{\mathrm{A}i}, c\kappa_{\mathrm{B}i}$, and β_i are set as free variables. In the following derivation, the coupling terms are static by dealing with the instantaneous picture of the driven Hamitonian and the system is examined at arbitrary values for the three aforementioned variables. If a degeneracy (a Dirac point) exists at an arbitrary $\boldsymbol{k}_D$ value between the pair of bands with eigenvalue β_0 (for the Hamiltonian involving all 3 chains), we can normalize the field intensities at β_0, ($\psi' = \psi e^{i\beta_0 t}$) so that the eigenvalue becomes zero at the degeneracy. This action leads to the following set of equations

$$\begin{aligned} \beta'\psi_{\mathrm{A}} &= \beta_0\psi_{\mathrm{A}} + c_{\mathrm{A}i}\psi_i, \\ \beta'\psi_i &= \beta_0\psi_i + \beta_i\psi_i + c_{\mathrm{A}i}^*\psi_{\mathrm{A}} + c_{\mathrm{B}i}\psi_{\mathrm{B}}, \\ \beta'\psi_{\mathrm{B}} &= \beta_0\psi_{\mathrm{B}} + c_{\mathrm{B}i}^*\psi_i. \end{aligned} \tag{S4}$$

By substituting the second expression of equations (S4) to the first and third, eliminating the term ψ_i, we reach a pair of equations that directly couple elements A and B. In matrix form,

$$\begin{bmatrix} \psi_{\mathrm{A}} \\ \psi_{\mathrm{B}} \end{bmatrix} = \begin{bmatrix} H_{11} & H_{12} \\ H_{21} & H_{22} \end{bmatrix} \begin{bmatrix} \psi_{\mathrm{A}} \\ \psi_{\mathrm{B}} \end{bmatrix}, \tag{S5}$$

$$H_{11} = \frac{\beta_0\beta_i + \beta_0^2 + |c_{\mathrm{A}i}|^2}{\beta_i + 2\beta_0}, \qquad H_{22} = \frac{\beta_0\beta_i + \beta_0^2 + |c_{\mathrm{B}i}|^2}{\beta_i + 2\beta_0}, \qquad H_{12} = \frac{c_{\mathrm{A}i}^* c_{\mathrm{B}i}}{\beta_i + 2\beta_0}, \qquad H_{21} = \frac{c_{\mathrm{B}i}^* c_{\mathrm{A}i}}{\beta_i + 2\beta_0}. \tag{S6}$$

To reach an ordinary form for the eigenproblem we omitted all second order terms of β', containing this derivation exclusively to a neighborhood of β_0 and therefore of $\boldsymbol{k}_D$. Here, we may also set $c_i = c_{\mathrm{A}i} = c_{\mathrm{B}i}$, considering that the elements A and B are identical, rendering the diagonal elements equal, $H_{11} = H_{22}$. This suggest that the instantaneous Hamiltonian will indeed maintain a gapless spectrum at the Dirac bands for arbitrary combinations of the couplings c_i ($i = 1,2,3$). To reach a form similar to equation (S2) we can analytically find the degeneracy point of the Dirac pair and linearize the system accordingly. We must note that for the initial assumption to remain accurate ($\beta' = 0$ at k_{D}) the diagonal terms must vanish, $H_{11} = H_{22} = 0$, after all three chain subsystems have been included into the 2×2 effective Hamiltonian, suggesting a close relation between β_0, c_i and β_i.

In this form, it is evident that the effective couplings between A and B are controlled by the inner hoping strength c_i and the detuning β_i, without the need to modify the main elements of the lattice in any way. This observation unlocks the possibility to change a number of fundamental properties of the Dirac cone, namely its location, anisotropy, velocity etc. In our case, during the Floquet drive the Dirac cone location is varied clockwise or counterclockwise in a small circle in k space infinitesimally close to k_{D}.

Supplementary Section S.II: *Numerical solutions to the time-periodic Schrödinger equation*

A solution to the time-dependent Schrödinger equation $i\partial_t|\psi(\boldsymbol{r},t)\rangle = \mathrm{H}_t|\psi(\boldsymbol{r},t)\rangle$ with a spatially and temporally periodic Hamiltonian H_t can be written in the Floquet form

$$|\psi(\boldsymbol{r},t)\rangle = e^{i\beta t}e^{i\boldsymbol{k}\cdot\boldsymbol{r}}|u(\boldsymbol{r},t)\rangle, \tag{S7}$$

with $|u(\boldsymbol{r},t)\rangle$ being periodic in both space and time with the same period as H_t. We seek solution to the following eigenvalue problem

$$\beta|u(\boldsymbol{r},t)\rangle = (\mathrm{H}_t - id_t)|u(\boldsymbol{r},t)\rangle. \tag{S8}$$

To calculate the quasi-spectrum of $(\mathrm{H}_t - id_z)$ we expand $|u(\boldsymbol{r},t)\rangle$ into a Fourier time series,

$$|u_n\rangle = [u_{sn}, u_{cn}] = \left[\tfrac{2}{T}\int_0^T \cos(2\pi nt/T)\,|u_t\rangle dt\,,\quad \tfrac{2}{T}\int_0^T \sin(2\pi nt/T)\,|u_t\rangle dt\right], \tag{S9}$$

where the sine and cosine inner product integrals result into two independent series with generalized complex coefficients u_{sn}, u_{cn}. Next, we calculate the inner products of $(\mathrm{H}_t - id_t)$ with the harmonic functions $\cos(2\pi nt/T)$ and $\sin(2\pi nt/T)$, in order to extract, in matrix form, the Hamiltonian that acts on the vector $|u_n\rangle = (u_n, u_{s1}, u_{c1}\ldots)$, labeled as H_F,

$$\mathrm{H}_F = \begin{bmatrix} H_0 & H_{0s1} & H_{0s1} & \cdots & H_{0sN} & H_{0cN} \\ H_{s10} & H_{s1} & H_{s1c1} + H_{\Lambda 1} & \cdots & H_{s1sN} & H_{s1cN} \\ H_{c10} & H_{c1s1} - H_{\Lambda 1} & H_{c1} & \cdots & H_{c1sN} & H_{c1cN} \\ \vdots & \vdots & \vdots & \ddots & \vdots & \vdots \\ H_{sN0} & H_{sNs1} & H_{sNc1} & \cdots & H_{sN} & H_{sNcN} + H_{\Lambda 1} \\ H_{cN0} & H_{cNs1} & H_{cNc1} & \cdots & H_{cNsN} - H_{\Lambda 1} & H_{cN} \end{bmatrix}, \tag{S10}$$

where N is the order up to which we truncate the matrix. The individual operators depend on H_t which in our case has the conventional form $\partial^2/\partial x^2 + \partial^2/\partial y^2 + V(x,y,t)$. The diagonal operators (H_0, H_{sn}, H_{cn}) are identical between the driven and the static case. In the static case the off-diagonal operators will be 0 ($H_{Fij} = 0$ for $i \neq j$) and the element of the $|u_n\rangle$ vector will be decoupled. In the driven case, the different elements of $|u_n\rangle$ interact through the off-diagonal operators, and the corresponding eigensolutions will dictate the modes of periodic evolution during the drive.

Here the problem is solved utilizing a finite difference method by direct discretization in the two spatial dimensions. For tilted unit cells, as in the case of the honeycomb lattice we also apply the transformation $(x' = x + y/\tan\theta, y' = y)$ to properly impose the periodic conditions in the $N_x, \times N_y,$ discretized space. The diagonal operators are matrices acting with non-zero elements according to the following equation

$$Au_{i,j} + Fu_{i,j+1} + Gu_{i,j-1} + Bu_{i+1,j} + Cu_{i-1,j} + Zu_{i-1,j-1} + Xu_{i-1,j+1} + Yu_{i+1,j-1} + Wu_{i+1,j+1} = \beta u_{i,j} \tag{S11}$$

where

$$\begin{gathered} A = V_{s/cn}(i,j,t) - 2(1+\tan^2\theta)/\Delta x^2 - 2/\Delta y^2 - k_x^2(1+\tan^2\theta) - k_y^2 + 2k_xk_y\tan\theta, \\ B = (1+\tan^2\theta)/\Delta x^2 + \left[ik_x(1+\tan^2\theta) - ik_y\tan\theta\right]/\Delta x, \\ B = (1+\tan^2\theta)/\Delta x^2 - \left[ik_x(1+\tan^2\theta) - ik_y\tan\theta\right]/\Delta x, \\ F = 1/\Delta y^2 + (ik_y - ik_x\tan\theta)/\Delta y, \quad G = 1/\Delta y^2 - (ik_y - ik_x\tan\theta)/\Delta y, \\ X = Z = -W = -Y = 2\tan\theta\,/\big(4k_xk_y\big) \quad V_{sn}(i,j,t) = \tfrac{2\pi}{T}\langle V(i,j,t)\sin(2\pi nt/T)\,|\,\sin(2\pi nt/T)\rangle, \end{gathered} \tag{S12}$$

Moreover, the off-diagonal operators in equation (S10) are given by diagonal matrices with elements

$$
\begin{aligned}
H_{\Lambda n} &= -\frac{i2\pi n}{T}, \\
H_{snsm} &= \frac{2\pi}{T}\langle V(i,j,t)\sin(2\pi nt/T) \mid \sin(2\pi mt/T)\rangle, \\
H_{sncm} &= \frac{2\pi}{T}\langle V(i,j,t)\sin(2\pi nt/T) \mid \cos(2\pi mt/T)\rangle, \\
H_{cnsm} &= \frac{2\pi}{T}\langle V(i,j,t)\cos(2\pi nt/T) \mid \sin(2\pi mt/T)\rangle, \\
H_{cncm} &= \frac{2\pi}{T}\langle V(i,j,t)\cos(2\pi nt/T) \mid \cos(2\pi mt/T)\rangle,
\end{aligned}
\tag{S13}
$$

with T the period of the drive and i, j the spatial discrete indices.

This formulation should be well suited for sinusoidal driving in the potential $V(t)$, providing a good threshold for safely truncating H_F to N terms. The solution to H_F will always produce N copies of Floquet bands with the middle group being the most numerically accurate. Through this technique, we calculate the band structure of the chained lattice, terminated along the y dimension. Each site has a Gaussian potential profile of order four with radius and magnitude set to match the experimental design.

In Fig. S3, we plot the eigenspectrum and select eigenmode solutions for both the static and driven case. In the driven case, only the first 3 elements of the u_{sn} vector are indicatively shown. Minor deviation can be observed for the flat-band states in the middle of the driven spectrum. These are attributed to the next-nearest neighbor coupling between adjacent chains which can been verified by including the corresponding terms in the tight-binding representation. However, the fundamental topological properties remain unaffected.

Supplementary Section S.III: *Berry phase calculation in the driven picture*

The Berry curvature is calculated numerically in the $\boldsymbol{k}$ space for each band n, according to the following definition

$$\Omega_n = i\sum_{m=1\,(m\neq n)}^{5} \frac{\langle\psi_n|\partial \mathrm{H_{eff}}/\partial k_x|\psi_m\rangle\langle\psi_m|\mathrm{H_{eff}}/\partial k_x|\psi_n\rangle - \langle\psi_n|\mathrm{H_{eff}}/\partial k_y|\psi_m\rangle\langle\psi_m|\mathrm{H_{eff}}/\partial k_y|\psi_n\rangle}{(\beta_n-\beta_m)^2}, \tag{S14}$$

where $\mathrm{H_{eff}}$ is the effective Hamiltonian in the tight-binding representation. The Chern number is then expressed as the total integral of Ω_n in the first Brillouin zone. In this context, Fig. S2 illustrates the Berry curvature for the first two bands and three different topological phases. Note that in the trivial topological phase with no drive the two cones cancel their contributions to C and the total invariant is zero, for both bands. When a small drive is applied, the topological charge of one of the two cones swaps sign. For the top band, each cone contributes $1/2$ to the invariant resulting in total $C = 1$. For the second band the two cones contribute $-1/2$ and the Chern number is expected to acquire the value $C = -1$, similarly to a diatomic honeycomb lattice. However, due to the interaction between the second band and the flat-band, during the period of the drive, a second gap opens and an opposite topological charge is generated at the middle of $\boldsymbol{k}$ space. This topological charge takes the value +1 which cancels the contribution of both cones combined for a new total $C = 0$.

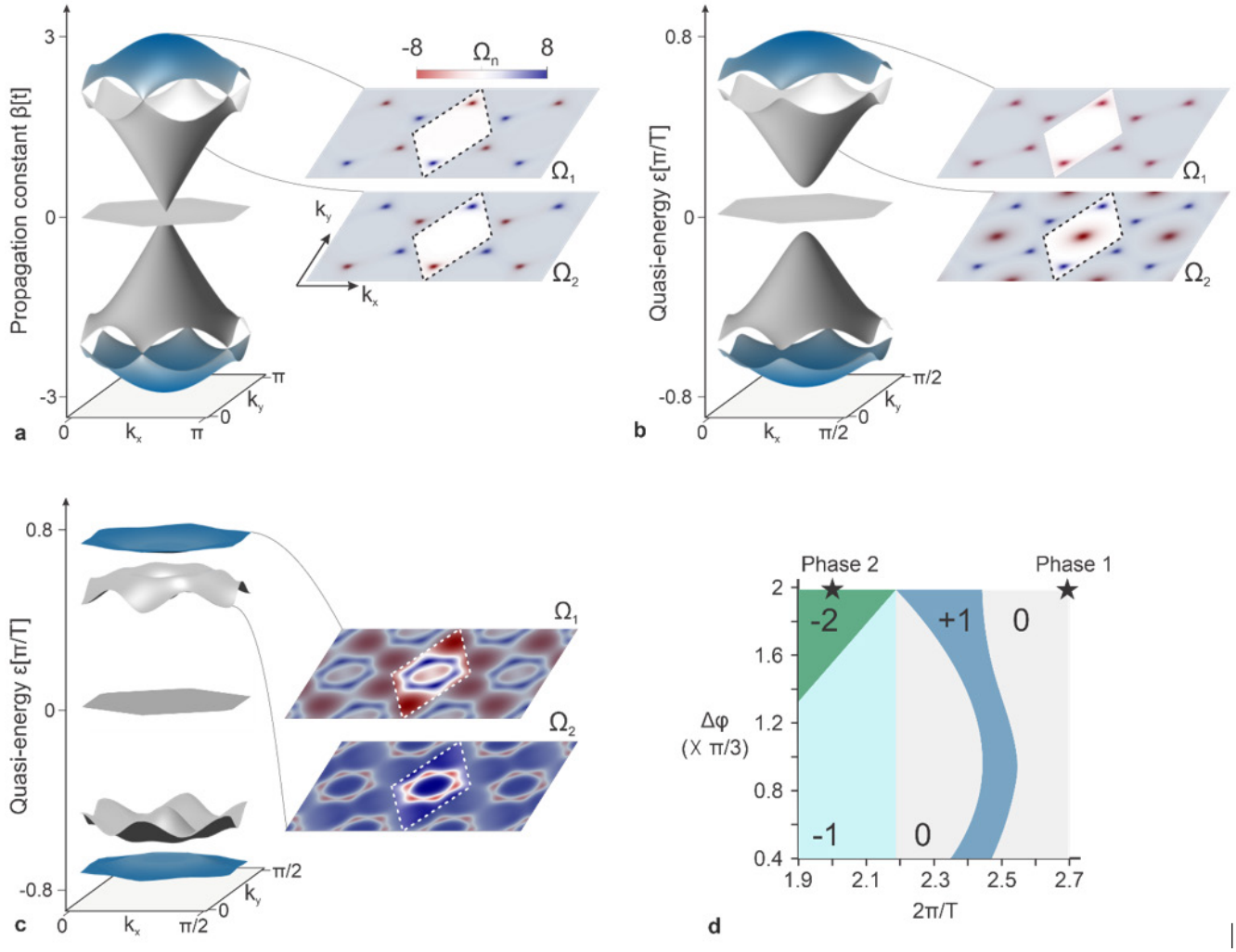

Figure S2: Bulk band structures and Berry curvature for various topological phases. (a) In the trivial topological phase (absence of periodic drive) the Berry curvature is antisymmetric and its integral yields a net zero Chern number. **(b)** When a non-trivial topological phase is induced ($2\pi/T = 6$) the Berry curvature yields a ∓ 1 Chern number for the blue shaded bands. **(c)** The overdriven lattice ($2\pi/T = 2$) manifests a highly complex Berry curvature in **k** space that yields Chern numbers with higher

integer values (∓ 2) for the white shaded bands. **(d)**. Phase diagram near the transition point of the higher Chern phase. The Chern number is depicted only for the second band over different periods of the drive and phase difference $\Delta\varphi$ between two chains. The band structures of (b) and (c) correspond to $\varphi = 2\pi/3$ at locations marked with stars.

In the third case, the Berry curvature is calculated for the second topological phase of the chained lattice shown in Extended Data Fig.3. Here, the picture is far more complex as multiple copies of the phase spectrum coalesce into the first Floquet zone and interact with each other. However, the integral of the topological invariant remains highly robust resulting in the integer values reported in Extended Data Fig.3.

In general, the complex topological structure observed for higher periods of the Floquet drive is a result of the intricate interactions between bands of different quasi-energy windows. In the simple case shown in Extended Data Figure XD2, where only two bands coexist in each window, a non-trivial interaction can occur only between the top band of quasi-energy window $[-\pi/T, \pi/T]$ and the bottom band of quasienergy window $[\pi/T, 2\pi/T]$, when the period T is high enough. This results in the emergence of edge states at the Floquet gap, near $\varepsilon = -\pi/T$ and $\varepsilon = \pi/T$, as shown in the third panel. The chained lattice of Extended Data Figure XD3 is much more complex as it involves a total of 5 bands. Now, the top (1st) band of quasi-energy window $[-\pi/T, \pi/T]$ and the bottom (5th) band of quasienergy window $[\pi/T, 2\pi/T]$ cannot interact. Instead, we need to increase the period T even more to allow an interaction between the 2st and the 4th bands. In this case, we can see from the 3rd panel of Extended Data Figure XD3 that the edge states must cut through the bulk bands in order to cross the Floquet gap at π/T and connect interacting bands between different Floquet quasi-energy windows. This justifies the presence of multiple edge states in each gap and the emergence of higher Chern numbers.

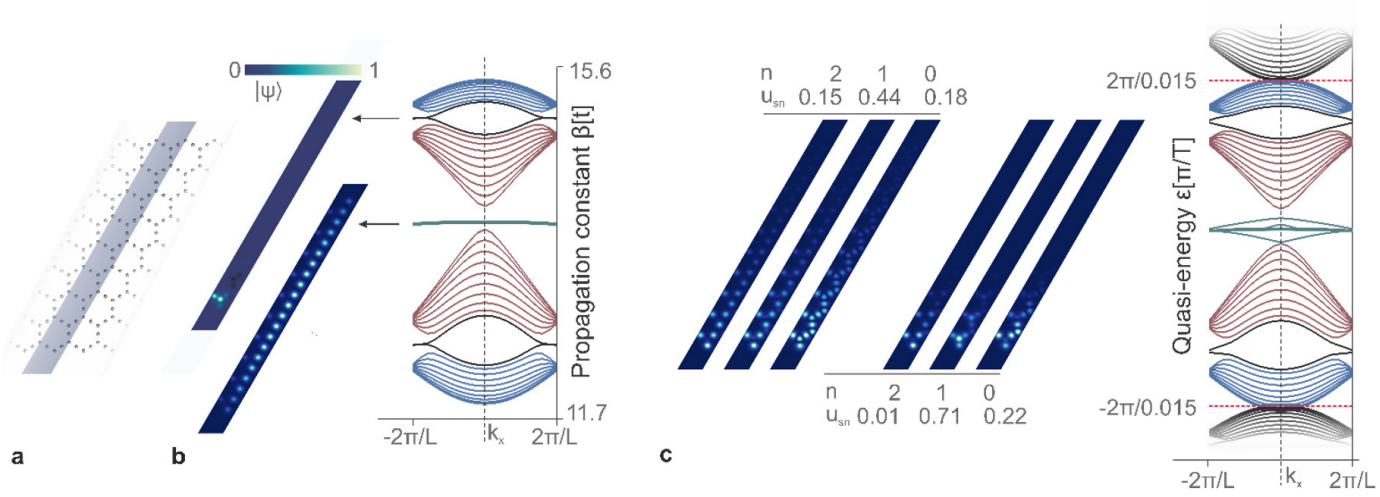

Figure S3: Band structures and Floquet eigenmodes for the time-periodic Schrödinger equation. (a) The ribbon unit cell. **(b)** The static system band structure with two eigenmode depicting a stationary edge state and a flat-band mode for a unit cell length in natural units $L = 26\mu m$. **(c)** Floquet band structure and two eigenmodes with normalized amplitude for the Chern edge state (left) and a flat-band edge state (right) for 3 terms of equation (S8).

Supplementary Section S.IV: *Excitation specifics and robustness against defects*

The symmetric Floquet spectrum of the bimorphic TI necessitates the existence of two Dirac bands. As illustrated in Fig. S4, the field amplitude of the upper-gap state is primarily localized on the central site of the unit cell, but features significant contributions with the same sign of the field on the adjacent chain sites as well. In contrast, chain-site amplitudes of the lower-gap state exhibit the opposite sign. The excitation employed in our experiments and simulations, being focused on the primary sites, therefore inevitably populates a superposition of these two states. Note that however, as the slopes of the Chern branches in the upper and lower gap are equal, the injected wave packet is not subject to dispersive broadening between its two components when it propagates along the edge. Selectivity between the Chern states of the upper and lower gap could in principle be achieved by directly synthesizing the internal field distributions of the desired mode. Similarly, widening the individual excitation beams to partially encompass the adjacent chain sites would likewise allow one to tilt the balance towards the upper-gap state. However, doing so would actually be detrimental to the confinement of the Chern wave packet, as the chain-site contributions only cancel perfectly for a 50:50 superposition of the two modes.

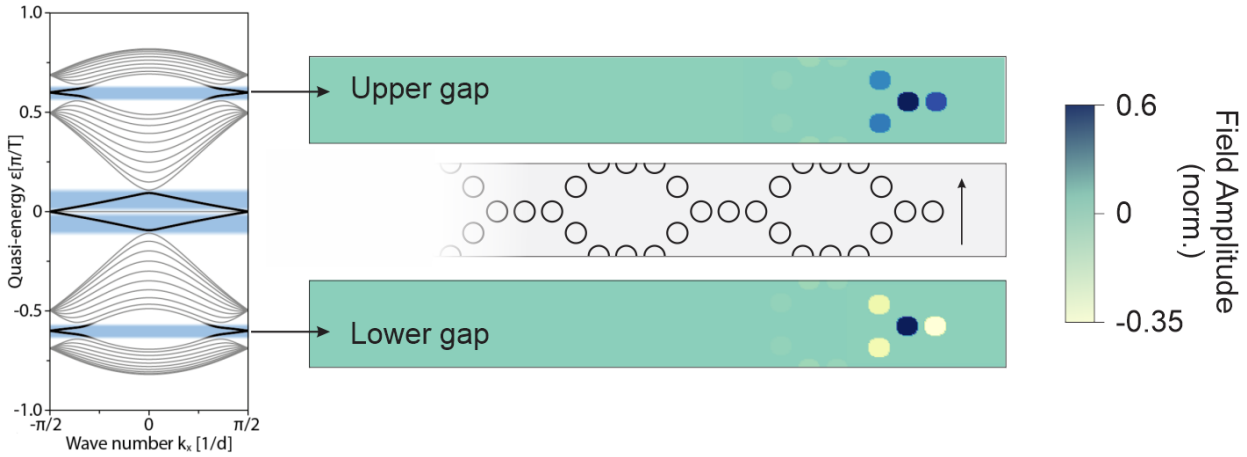

Figure S4: Comparison of the field distributions of the topological modes in the upper and lower Chern gaps. Whereas all waveguides of a unit cell are in phase for the state in the upper gap, its lower-gap counterpart is characterized by opposite signs of the field in the central cite compared to the auxiliary chain sites. The absolute value of the individual field distributions is identical in both cases, and the superposition of both modes effectively cancels the chain-site contributions of the Chern edge channel, effectively separating it from the anomalous channel.

The amplitude distributions of the different Chern modes in the $C = 2$ phase are shown in Fig. S5. In this super-critically driven regime, the edge modes of the $C = 1$ regime persist as inner states and carry over a similarity of the absolute values of their field amplitude distributions between the upper and lower gaps. The outer state (red line) features a more involved field distribution with substantial population on the chain sites, nevertheless preserving the symmetry of the intensity patterns between upper and lower gap. Long-range BPM simulations show that, due to the different slopes of the inner and outer states, a wave packet injected into the Chern edge channel as superposition of the two is subject to substantial dispersive broadening over longer propagation distances in the $C = 2$ phase, and eventually breaks into separate wave packets that correspond to the individual excited states. However, the confinement to the edge of the system remains intact.

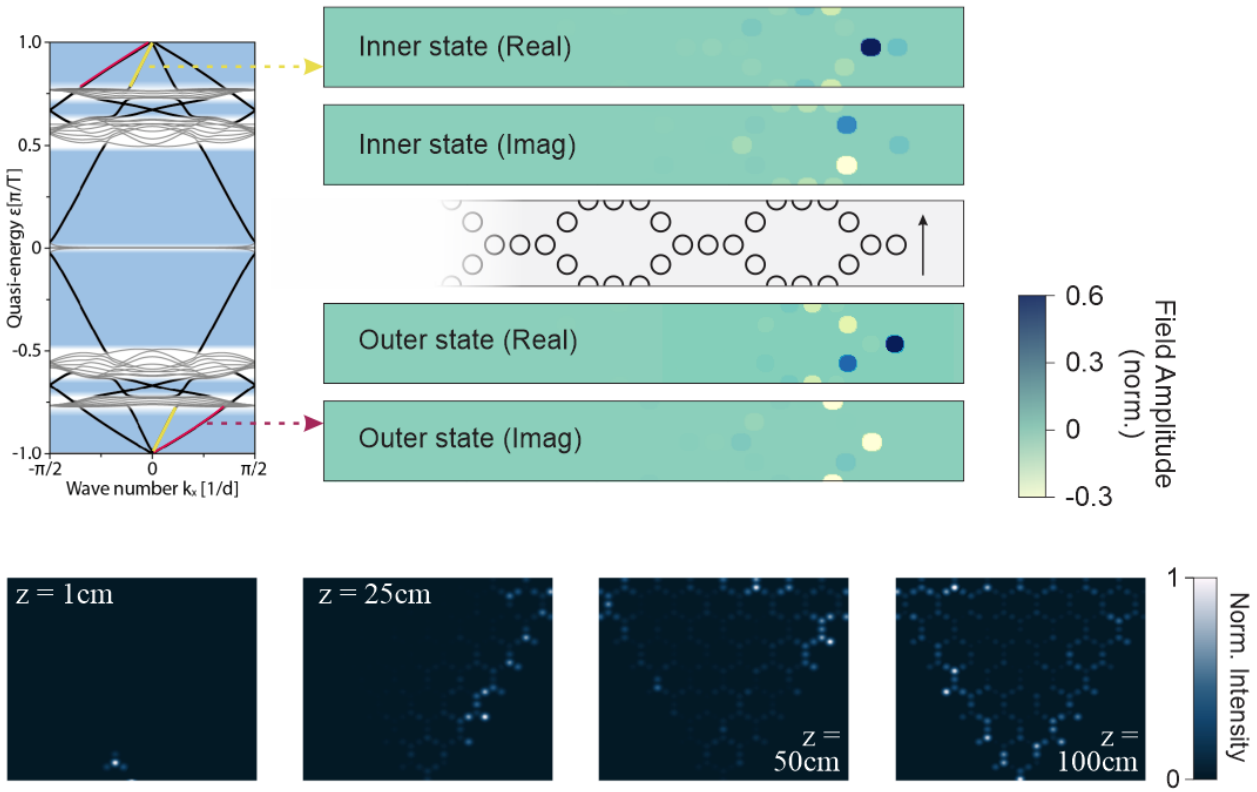

Figure S5: Mode amplitudes and propagation simulations in in the $C = 2$ phase. Top: The inner state (yellow line) in this regime emerges from the Chern mode of the $C = 1$ phase and inherits its localization on the primary sites as well as the symmetry of its intensity distributions between the upper and lower gaps. Whereas all waveguides of a unit cell are in phase for the state in the upper gap, its lower-gap counterpart is characterized by opposite signs of the field in the central cite compared to the auxiliary chain sites. The absolute value of the individual field distributions is similar in both cases, and the superposition of both modes effectively reduces the chain-site contributions of the Chern edge channel, although not as fully as in the $C = 1$ phase (c.f. Fig. S4 above). The outer state (red line) features a more involved field distribution with substantial population on the chain sites, nevertheless preserving the symmetry of the intensity patterns between upper and lower gap. Bottom: As a result, a wave packet injected into the Chern edge channel is subject to substantial dispersive broadening over longer propagation distances. However, the confinement to the edge of the system remains intact.

The chained honeycomb lattice exhibits a similar level of robustness to other types of topological lattices. In the context of photonic waveguide arrays, it is comparable in this respect to a helical waveguide array which is commonly employed for topological experiments. Meanwhile, it offers further advantages considering that the inevitable radiation losses of the conventional driving schemes are entirely avoided. To showcase this robustness, we conducted BPM simulations of the anomalous edge mode in the presence of for three common defect types with different shapes that demonstrate the level of topological protection in the lattice (Fig. S6). The three panels of each subfigure correspond to three propagation lengths; at the beginning of the simulation, before the defect and after passing the defect. In all cases the edge excitation finds an alternative path around the defect with negligible bulk scattering.

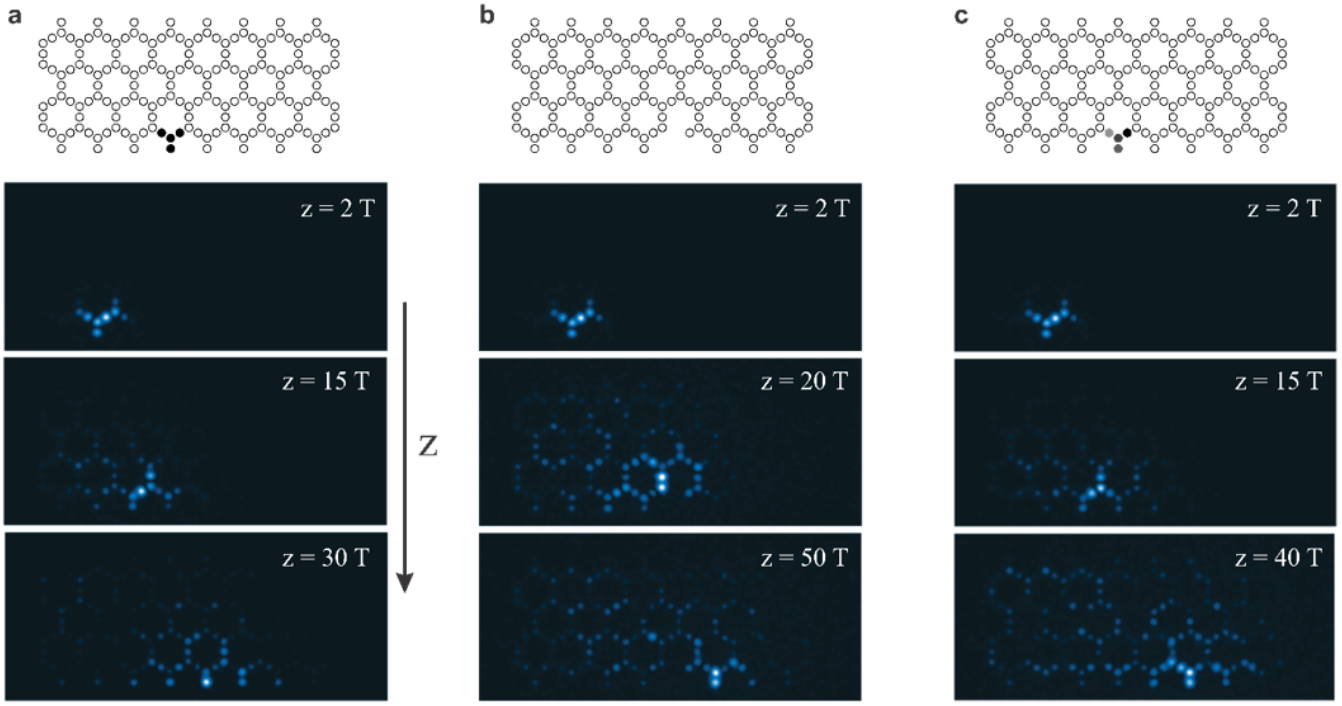

Figure S6: Robustness against defects. Three common defect cases that demonstrate the level of topological protection in the lattice. Regardless of whether **(a)** the periodic modulation is locally disabled (static region marked in black), **(b)** a number of waveguides is missing along the edge, or **(c)** a random static on-site potential is added to the waveguides (marked in gray, up to 20% Δn), the chiral edge state is able to circumnavigate the defect region without backscattering.

In the Supplementary video, we numerically demonstrate how two anomalous wave packets propagating along the edge channel can be efficiently reshuffled by suspending the Floquet drive in a single unit cell. In this vein, the topological edge wave packet therein is temporarily converted into a compact localized flat-band state and held in place until the modulation is resumed. Given proper timing, this process can be executed virtually without scattering losses, and furthermore demonstrates the robustness to modulation defects for the wave packet that is allowed to overtake the stationary one.